# Journal Pre-proof

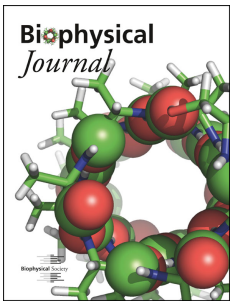


$\alpha_{IIb}\beta_3$ integrin intermediates: from molecular dynamics to adhesion assembly

Dudu Tong, Nidhi Soley, Reza Kolasangiani, Martin A. Schwartz, Tamara C. Bidone

PII: S0006-3495(22)03942-X

DOI: https://doi.org/10.1016/j.bpj.2022.12.032

Reference: BPJ 12312

To appear in: *Biophysical Journal*

Received Date: 31 January 2022

Accepted Date: 21 December 2022

Please cite this article as: Tong D, Soley N, Kolasangiani R, Schwartz MA, Bidone TC, $\alpha_{IIb}\beta_3$ integrin intermediates: from molecular dynamics to adhesion assembly, *Biophysical Journal* (2023), doi: https://doi.org/10.1016/j.bpj.2022.12.032.

# $\alpha_{IIb}\beta_3$ integrin intermediates: from molecular dynamics to adhesion assembly

Dudu Tong[1,2,#], Nidhi Soley[1,2,#], Reza Kolasangiani[1,2], Martin A. Schwartz[3,4,5], Tamara C. Bidone[1,2,6,7*]

[1]Department of Biomedical Engineering, University of Utah, Salt Lake City, Utah

[2]Scientific Computing and Imaging Institute, University of Utah, Salt Lake City, Utah

[3]Yale Cardiovascular Research Center, Department of Internal Medicine (Cardiology), Yale University, New Haven, Connecticut

[4]Department of Cell Biology, Yale University, New Haven, Connecticut

[5]Department of Biomedical Engineering, School of Engineering and Applied Science, Yale University, New Haven, Connecticut

[6]Department of Biochemistry, University of Utah, Salt Lake City, Utah

[7]Department of Molecular Pharmaceutics, University of Utah, Salt Lake City, Utah

*** Corresponding author**: Tamara C Bidone (tamarabidone@sci.utah.edu)

**# These authors contributed equally to this work**

**Date:** 12/23/22

## Abstract

The platelet integrin $\alpha_{IIb}\beta_3$ undergoes long range conformational transitions associated with its functional conversion from inactive (low affinity) to active (high affinity) states during hemostasis. Although new conformations intermediate between the well-characterized bent and extended states have been identified, their molecular dynamic properties and functions in the assembly of adhesions remain largely unexplored. In this study, we evaluated the properties of intermediate conformations of integrin $\alpha_{IIb}\beta_3$ and characterized their effects on the assembly of adhesions by combining all-atom simulations, principal component analysis, and mesoscale modeling. Our results show that in the low affinity, bent conformation, the integrin ectodomain tends to pivot around the legs; in intermediate conformations the upper headpiece becomes partially extended, away from the lower legs. In the fully open, active state, $\alpha_{IIb}\beta_3$ is flexible and the motions between upper headpiece and lower legs are accompanied by fluctuations of the transmembrane helices. At the mesoscale, bent integrins form only unstable adhesions, but intermediate or open conformations stabilize the adhesions. These studies reveal a mechanism by which small variations in ligand binding affinity and enhancement of the ligand-bound lifetime in the presence of actin retrograde flow stabilize $\alpha_{IIb}\beta_3$ integrin adhesions.

## Significance Statement

Precise regulation of the affinity state of integrin $\alpha_{IIb}\beta_3$ is critical for health; failure to activate underlies bleeding disorders whereas excessive activation triggers blood clotting. However, conformational transitions for $\alpha_{IIb}\beta_3$ activation remain incompletely understood. In this study, we show that integrin structures that are intermediate between the well-known bent and extended states control the stability of nascent adhesions through changes in atomistic motions that underlie differences in ligand-binding affinity. These results are conceptually important because they identify new functional relationships between integrin conformation and cell function.

## Introduction

The integrin $\alpha_{IIb}\beta_3$ is expressed at high density on the surface of blood platelets and is indispensable for hemostasis via its binding to fibrin, fibrinogen, and other extracellular matrix proteins (1). In unstimulated platelets, integrin $\alpha_{IIb}\beta_3$ is held in a bent conformation with almost negligible affinity for these ligands; upon stimulation and activation of platelets, affinity for these ligands increases up to the nanomolar range, coincident with transitions to extended conformations. Mutations that prevent activation lead to a bleeding disorder, Glanzmann's thrombasthenia (2). Conversely, increased activation state is linked to thrombotic disease, for which $\alpha_{IIb}\beta_3$ antagonists are in clinical use (3).

Integrins are transmembrane heterodimers formed by the noncovalent association of an α and a β chain. Their inactive/bent and active/extended states have been described (4–7); however, interconversion between these states necessarily involves intermediate conformations that are less well studied. Such intermediates have been observed for $\alpha_{IIb}\beta_3$ and present different degrees of extension of the ectodomain (Figure 1a-d) (8–11). The extracellular region of integrin $\alpha_{IIb}\beta_3$ consists of a large ectodomain divided into headpiece and lower legs (Figure 1e). The $\alpha_{IIb}$ headpiece contains an N-terminal β-propeller domain, followed by the thigh domain; the $\alpha_{IIb}$ leg contains two calf domains (Figure 1e). The $\beta_3$ headpiece consists of an N-terminal β-I domain followed by the hybrid domain and the plexin-semaphorin-integrin (PSI) domain; the $\beta_3$ leg includes four cysteine-rich epidermal growth factor (I-EGF) modules 1-4 and the β-T domain (Figure 1e). Each of these extracellular regions is followed by a single membrane spanning helix ending with a C-terminal cytoplasmic tail that binds to cytoskeletal linkers and adapters.

In the bent conformation, the α and β chains are close together, with the headpiece bent against the lower legs (Figure 1a and 1f); in the open conformation (Figure 1d), the headpiece is separated from the lower legs and the α and β chains are apart (Figure 1d). Different integrin intermediates present different degrees of headpiece extension, but the lower α and β legs and transmembrane helices remain close together (Figure 1b-c) (8–10). $\alpha_{IIb}\beta_3$ integrin intermediates present ligand binding affinities and ligand-bound lifetimes that are in between the bent and extended conformations and these molecular properties associate with different levels of cell adhesiveness (8, 11–13). Elucidating the properties of integrin $\alpha_{IIb}\beta_3$ intermediates and characterizing their contributions to the assembly of adhesions is important for understanding the regulation of hemostasis in molecular detail and integrin regulation more generally.

Integrins behave like mechanical springs (14). When bound to a ligand, the integrin spring constant is lower for bent than open conformations. However, in the unbound state extended integrins show higher flexibility relative to the bent conformations (15), supporting the idea that stabilization of the extended conformation occurs through ligand binding (16, 17). How intermediate conformations of $\alpha_{IIb}\beta_3$ integrin impact the assembly of adhesions remains largely unknown. To understand the role of the molecular properties of integrin intermediates in the assembly of adhesions, here we combined molecular simulations with mesoscale modeling.

We first performed equilibrium molecular dynamics (MD) simulations of membrane-embedded $\alpha_{IIb}\beta_3$ integrins in bent, extended and intermediate conformations. Then, we evaluated residue fluctuations and analyzed the principal components of residue motions. Last, we incorporated integrin intermediates into a mesoscale model of adhesion

assembly to analyze how they affect the stability of adhesions. Our results showed that the structural deformations of the bent and intermediate conformations are directed toward elongation of the headpiece away from the legs, and destabilization of the transmembrane helices; the open conformation presents high flexibility, with correlated motions between headpiece and legs. Additionally, we found that bent integrins cannot form stable adhesions, but intermediate or open conformations stabilize the adhesions. These effects are due to small variations in ligand binding affinity and ligand-bound lifetime in the presence of actin retrograde flow.

## Methods

We started with cryo-EM $\alpha_{IIb}\beta_3$ integrins in the bent, extended and intermediate conformations. These structures were purified from human platelets and embedded in lipid nanodiscs with talin and RGD bound for the cryo-EM study (18). We ran 500 ns of equilibrium MD simulations and calculated the residue and domain fluctuations, which allowed us to assess local differences in dynamics between the different conformations. Then, from an evaluation of the principal components of residue motions, we characterized the emergent displacements and the extensional stiffnesses governing the energy well of each conformation. From an analysis of extensional stiffnesses we estimated the rates for ligand binding and incorporated these parameters into our mesoscale model. Finally, we used a mesoscale model to study how $\alpha_{IIb}\beta_3$ conformations affect the average percentage of ligated integrins in nascent adhesions and their stability.

## All-atom molecular dynamics simulations

We first reconstructed the missing residues in each of the four $\alpha_{IIb}\beta_3$ cryo-EM conformations (see Supplementary Information and Figure 1g-j). The completed structures of bent, intermediates (int1 and int2), and open $\alpha_{IIb}\beta_3$ integrin were embedded within a DOPC+DOPS lipid bilayer with a molar ratio of 3:1, using the CHARMM-GUI membrane builder (21) (an example is shown in Figure 1f). Each $\alpha_{IIb}\beta_3$ integrin conformation was oriented so that the transmembrane α helix was perpendicular to the lipid bilayer (22–24). The integrin/membrane systems were solvated using CHARMM-modified TIP3P water model (25) and 150 mM NaCl. The sizes of each box were: 15.07 x 15.07 x 24.34 nm for bent integrin; 12.85 x 12.85 x 26.31 nm for int1; 13.16 x 13.16 x 31.16 nm for int2; and 16.10 x 16.10 x 33.82 nm for the open integrin. The solvated systems contained approximately: 523,000 total atoms for the bent conformation, 443,000 atoms for int1, 599,000 atoms for int2 and 836,000 atoms for the open conformation. The number of molecules of the different species (lipids, water, ions, and protein) is reported in Supplementary Table 2.

The systems were energy minimized using the steepest descent algorithm, followed by two consecutive equilibration simulations in the constant NVT ensemble (constant number of atoms, $N$, volume, $V$, and temperature, $T$ = 310 K) and four consecutive equilibration simulations in the constant NPT ensemble (constant number of atoms, $N$, pressure, $P$, and temperature, $T$ = 310 K). These equilibration simulations gradually reduced the restraining potentials of the backbone atoms (parameters listed in Supplementary Table 3).

The production runs were then continued in the constant NPT ensemble at 310 K and 1 atm using the velocity rescaling thermostat and the isotropic Parrinello-Rahman pressure coupling (26). The length of the covalent bonds involving hydrogen atoms was constrained using the LINCS algorithm (27), allowing a time step of 2 fs. The Lennard-Jones interactions were cut off at 1.2 nm with a switching function ranging from 1.0 to 1.2 nm, and the short-range electrostatic cutoff was set at 1.2 nm. The long-range electrostatic interactions were computed using the particle-mesh Ewald (PME) method with a 0.16 nm grid spacing (28).

VMD and PyMol were used for the visualization of the simulation trajectories (29, 30). Gromacs analysis tools, combined with home-made scripts, were employed for the quantitative analysis of the trajectories.

**Fluctuation analysis using PCA essential modes**

PCA was performed on the $\alpha_{IIb}\beta_3$ integrin conformations using the Gromacs analysis tool “covar”. PCA analyzed the atomistic trajectories and decomposed the frame-by-frame conformational fluctuations of each protein residues (every 1 ns). For each conformation, it first aligned each frame to the first one, and then constructed the $3N$ x $3N$ covariance matrix for the $N$ alpha carbons, Cα, using the averaged structure. The eigenvectors and eigenvalues were calculated to assess the principal components and their associated variance. The principal components were then ordered so that the first accounted for the largest variance and the following components accounted for lower and lower variances.

From these modes, motions of the ectodomain we evaluated as fluctuations between the ligand binding site (pulling group) and transmembrane helices (reference group). From these modes, the extensional stiffness governing the energy well that maintained each integrin in its conformation was assessed. The distance fluctuations were calculated as:

$$D_F = \sum_{k=1}^{M} \lambda^k \left( \sum_{j=xyz} \frac{x_{1j} - x_{2j}}{s} \left( v_{1j}^k - v_{2j}^k \right) \right)^2 \quad (1)$$

where $\lambda^k$ and $v^k$ were the eigenvalue and eigenvector of $k$-th principal mode, $s$ was the distance between the centers of mass (COM) of the pulling and reference groups, and $M$ was the number of essential modes used to evaluate the distance fluctuations. $x_j$ was the $x$, $y$ or $z$ component of the COM coordinate of each group. $v_j$ was the $x$, $y$ or $z$ component of the eigenvector of each group. The effective extensional stiffness maintaining each integrin in its conformation was evaluated as:

$$k = \frac{k_B T}{D_F} \quad (2)$$

where $k_BT$ = 4.11 pN nm and $T$ = 310 K ($k_B$ is the Boltzmann constant and $T$ is the temperature).

**Brownian dynamics simulations of integrin adhesions assembly**

To elucidate how the four integrin conformations affect the assembly of adhesions, we used our molecular clutch-based model based on Brownian Dynamics, BD (31, 32). The simulation domain was 3D and included two parallel surfaces of 1 μm side, separated by a vertical distance $L$ = 20 nm (schematics in Figure S1a). The top surface represented the cell membrane, where integrins underwent lateral diffusion. The bottom surface presented randomly distributed ligands providing anchor points for integrin motion.

Integrins existed in two states: inactive and active. Inactive integrins on the top surface were diffusing particles obeying the overdamped Langevin equation, in the limit of high friction:

$$\boldsymbol{F_i} - \zeta_i \frac{d\boldsymbol{r_i}}{dt} + \boldsymbol{F_i^T} = 0 \quad (3)$$

where $\boldsymbol{r_i}$ was the position vector of the $i$-th integrin; $\zeta_i$ was the friction coefficient equal to 0.0142 pN s/μm, corresponding to the diffusion coefficient of integrin $\beta_3$ as $D$ = 0.29 μm$^2$/s (33), using Einstein relation $\varepsilon_i = \frac{k_B T}{D}$ ; $dt$ was the simulation timestep of 10$^{-4}$ s; and $\boldsymbol{F_i}$ and $\boldsymbol{F_i^T}$ were deterministic and stochastic forces, respectively.

For each inactive integrin within 21 nm from a free ligand, activation occurred at a rate $k_{on}$. The probability of ligand binding was:

$$P = 1 - e^{-k_{on} dt} \quad (4)$$

Once in the active and ligated state, each integrin *i* was subjected to a deterministic force $\boldsymbol{F_i}$, corresponding to the sum of the forces from the retrograde actin flow, $\boldsymbol{F_{flow}}$, and substrate, $\boldsymbol{F_{sub}}$:

$$\boldsymbol{F_i} = \boldsymbol{F_{flow}} + \boldsymbol{F_{sub}} \quad (5)$$

where $\boldsymbol{F_{flow}} = \zeta_i \boldsymbol{v}$, with $\boldsymbol{v}$ = 30 nm/s, and $\boldsymbol{F_{sub}}$ depended on substrate rigidity as:

$$\boldsymbol{F_{sub}} = \frac{YA}{L}\Delta \boldsymbol{L} \quad (6)$$

where *A* was the cross-sectional area of the integrin/ligand bond (from an ideal bar of radius ~5 nm, corresponding to half the separation between integrin transmembrane helices when extended); *Y* was the substrate Young's modulus (*Y* = 12.6 kPa); *L* = 20 nm was the equilibrium distance; and $\Delta L$ was the deviation from the equilibrium distance (18).

The stochastic force on each *i*-th integrin, $\boldsymbol{F_i^T}$, represented the thermal force generating Brownian motion. It satisfied the fluctuation-dissipation theorem (38), as:

$$\langle \boldsymbol{F_i^T}(t)\boldsymbol{F_j^T}(\boldsymbol{t})\rangle = \frac{2k_B T\zeta_i\delta_{ij}}{\mathrm{d}t}\boldsymbol{\delta} \quad (8)$$

where $k_B$ is the Boltzmann constant, $T$ is the temperature, $\delta_{ij}$ is the Kronecker delta and **δ** is a unit second-order tensor.

Unbinding of integrins was governed by catch bond kinetics (39, 40) in which the bond lifetime, $\tau$, depended on force, $\tau = f(\boldsymbol{F_{sub}})$ (Figure S1b). The unbinding rate, $k_{off}$, was calculated as:

$$k_{off} = A\, e^{-\alpha \boldsymbol{F_{sub}}} + B e^{\beta \boldsymbol{F_{sub}}} \quad (9)$$

Catch bond parameters were estimated from (8) and are listed in Supplementary Table 4. For each ligated integrin, the unbinding probability was:

$$P = 1 - e^{-k_{off}dt} \quad (10)$$

Our model used specific combinations of $k_{off}$ and $k_{on}$ to mimic each integrin conformation. $k_{off}$ and $k_{on}$ were provided as inputs and remained fixed to isolate integrin conformation from other factors, such as ligand binding or forces from substrate and actin.

For the bent conformation, the model used a minimum $k_{off}$ =0.16 $s^{-1}$ (maximum lifetime $\tau_{MAX}$= 6 s); for int1 a minimum $k_{off}$ = 0.09 $s^{-1}$ ($\tau_{MAX}$= 11 s); for int2 and open, $k_{off}$ = 0.04 $s^{-1}$ ($\tau_{MAX}$ = 22 s). $k_{on}$ was estimated from the extensional stiffnesses extracted from equation (2). Considering that the extensional stiffness of a protein is inversely related to the heigh of the free energy barrier for conformational change (40), we used, for the bent conformation, $k_{on}$ = 0.07 $s^{-1}$; for int1, $k_{on}$ = 0.7 $s^{-1}$; and for Int2 and the open conformations, $k_{on}$ = 1 $s^{-1}$. For each integrin conformation, ligand binding affinity, *E*, was calculated from $k_{off}$ and $k_{on}$, as free energy for binding, using $\frac{k_{off}}{k_{on}} = e^{-E}$.

Integrins' displacements were computed using explicit Euler integration scheme (41):

$$\boldsymbol{r_i}(t+dt) = \boldsymbol{r_i}(t) + \frac{d\boldsymbol{r_i}}{dt}dt = \boldsymbol{r_i}(t) + \frac{\boldsymbol{F_i^T} + \boldsymbol{F_i}}{\zeta_i}dt \quad (11)$$

## Code and data availability

A description of the implementation algorithm is provided in the Supplementary information. All MD trajectory files, the analysis code used for PCA, the code developed for the mesoscale model, and all input files, scripts and output data are publicly available at https://github.com/tamarabidone/multiscale-model-alphaIIbBeta3

## Results

### Atomistic simulations of different integrin conformations in lipid bilayers

Based on root mean square displacements of the alpha carbons, Cα, all conformations reached equilibrium within 300 ns (Figure 2a). Equilibrium Cα root mean square displacements (RMSDs) for the bent $\alpha_{IIb}\beta_3$ conformation were between 0.5-1 nm (Figure 2a). Cα RMSDs for the open $\alpha_{IIb}\beta_3$ conformation leveled off between 2-2.5 nm (Figure 2a). For Int1 and int2, Cα RMSDs reached equilibrium between 1.5-2 nm (Figure 2a), intermediate between bent and extended conformations. The radius of gyration was 4.5-5 nm for bent $\alpha_{IIb}\beta_3$, 6-7 nm for Int1 and Int2, and around 7 for open $\alpha_{IIb}\beta_3$, (Figure 2b). Analysis of RMSFs for each domain in $\alpha_{IIb}$ and β3 (Figure 2c) showed that the bent $\alpha_{IIb}\beta_3$ conformation is more stable than the open one, with the two intermediate conformations in between (Figure 2c). RMSFs for individual domains within Int2 were generally larger than for int1, except for the β-I and β-T domains. The greater fluctuations of β-I and β-T in int1 relative to int2 suggest possible destabilization of the β-I/β-T interactions in the initial phases of integrin extension, which are then stabilized as extension proceeds.

Residues' root mean square fluctuations (RMSFs) were between 0.1 and 2 nm (Figure S2a). Consistent with the RMSD analysis, RMSFs values were lowest for bent $\alpha_{IIb}\beta_3$ and highest for the open $\alpha_{IIb}\beta_3$ conformation, with Int1 and Int2 in between (Figure S2a). The RMSFs computed between 0-200 ns, 200-400 ns, and 300-500 ns ranged between 0.5-3.5 nm (Figure S2b-d). The overall distribution of RMSFs for each conformation decreased with time (Figure S2e), indicating stabilization of the structures.

The solvent accessible surface area (SASA) was approximately constant over time for bent $\alpha_{IIb}\beta_3$ integrin, Int1 and Int2, with values centered around 950 $nm^2$, but dropped below 900 $nm^2$ for open $\alpha_{IIb}\beta_3$ (Figure S2f). This reduction in SASA was due to the formation of noncovalent interactions between β-propeller and β-I domains in open $\alpha_{IIb}\beta_3$. Because the ligand binding site was free, sites for molecular contacts were available, which resulted in formation of new headpiece interactions. Taken together, results from equilibrium atomistic simulations of four $\alpha_{IIb}\beta_3$ integrin conformations revealed that the bent integrin is more stable than the open integrin, with the intermediate conformations presenting levels of residue and domain fluctuations generally between bent and open conformations.

In order to understand the effects of force and ligand binding on the motions of residues of $\alpha_{IIb}\beta_3$ integrin, we ran constant force steered molecular dynamics simulations on the bent conformation in the presence and absence of an RGD peptide. The overall residue motions increased with force magnitude (Figure S3); however, the most flexible regions in the structure did not change. By increasing force, the values of RMSD, radius of gyration and RMSF proportionally increased (Figure S3a-c). However, the RMSF peaks, indicating regions of high flexibility, were maintained at all forces (Figure S3c) and comparable to the force-free conditions (Figure S2a-d). The SASA of bent $\alpha_{IIb}\beta_3$ remained constant under force, with values centered around 950 $nm^2$ (Figure S3d). Additionally, like the force-free conditions, domain fluctuations under force generally increased from the β-propeller domain and from the β-I domain to the α and β transmembrane helices (Figure S3e). Using an RGD-bound headpiece, RMSD, RMSF, radius of gyration, SASA and the RMSF did not significantly change relative to the ligand-free conditions (Figure

S4). In the absence of plasma membrane lipids, the average RMSD, RMSF and radius of gyration of the integrin differed either not at all or only slightly from the membrane-embedded cases (Figure S5).

Collectively, our results showed that force enhances but does not significantly alter the residue fluctuations. Ligand binding or bound lipids also don't significantly affect these motions. These results point towards the general notion that the integrin atomistic motions are intrinsic properties of the structure and do not depend on force, lipids or ligand binding, although force can increase these motions.

**PCA of atomistic MD trajectories for different integrin conformations**

We performed PCA to identify the dominant modes of motion in the four $\alpha_{IIb}\beta_3$ integrin conformations. PCA identifies the essential dynamics of a system from a decomposition process that filters the motions into a few emergent structural deformations (48, 49). Out of thousands of modes, only a few modes accounted for more than half of the total fluctuations. The first few modes of all four $\alpha_{IIb}\beta_3$ conformations contained more than 40% of the total variance of Cα fluctuations (Figure 3a). For the bent $\alpha_{IIb}\beta_3$ integrin and int1, the first 3 modes contained more than 95% of the total variance (Figure 3a). For Int2 and the open conformation, the first or the first 8 modes contained more than 95% of the total variance, respectively (Figure 3a). Analysis of MD simulation trajectories between 0-300 ns, 200-500 and 300-500 ns, showed that the first 3 modes consistently contained more than 90% of the total variance for bent, int1 and int2 (Figure S6). For the open conformation, more than 80% of the total variance was contained in the

first 7 modes (Figure S6). Analysis of the distances between the COM of pulling and reference groups showed their convergence within the first mode for int2, within 3 modes for the bent conformation and int1 and within 8 modes for the open conformation (Figure 3b). This finding confirms that the bent conformation is the most stable and the open one the least stable. The effective force constant describing the extensional stiffness of integrin was about 2.5 x $10^5$ pN/μm for bent $\alpha_{IIb}\beta_3$ and ~10x lower for the intermediate and open conformations (Figure 3c). An evaluation of the extensional stiffness from the distances between pulling and reference groups detected values comparable to PCA, further indicating enhanced flexibility of the intermediate and open conformations with respect to the bent conformation (Figure S7). The high stiffness of the bent conformation indicates a high energy barrier for transitioning into the extended state, which is lower for the intermediate conformations, consistent with our previous results (15). The distance between the pulling and reference groups were around 8 nm for the bent integrin, 13 nm for int1 and 16 nm for int2 (Figure 3d). By contrast, in the open $\alpha_{IIb}\beta_3$ integrin, this distance initially increased from 15 to 20 nm, and then decreased and plateaued around 14 nm (Figure 3d). Collectively, PCA showed that the first few principal modes captured most of the Cα fluctuations and are thus representative of the emergent structural deformations of integrin. The bent and intermediate conformations showed higher variance for the first modes, indicating highly correlated motions, whereas the open conformation showed Cα fluctuations that were spread across different modes, indicating more complex dynamics.

**Identification of conformational clusters from projection of atomistic MD trajectories to PCA modes**

Since relatively few PCA modes captured the emergent dynamics of the four $\alpha_{IIb}\beta_3$ conformations, the MD simulation trajectories were projected onto the planes identified by the first and second principal modes. We used MDAnalysis, a Python package with an interactive object-oriented interface (50, 51). First, for each $\alpha_{IIb}\beta_3$ integrin conformation, we identified conformational clusters in the PCA plane (Figure 4). Then, we assessed the directions of the residue motions by superimposing the representative $\alpha_{IIb}\beta_3$ integrin conformations of each cluster and evaluating differences in residue positions (Figure 5).

For the bent $\alpha_{IIb}\beta_3$ integrin, we found two clusters (Figure 4a). Structures representative of these clusters showed a bending motion of the entire ectodomain around its membrane-proximal region, along the first principal mode (Figure 5a and Supplementary Movie 1). For int1, this analysis identified four clusters (Figure 4b). The comparison between structures of cluster 1 and 2, along the second principal mode, showed an opening of the headpiece relative to the lower legs (Figure 5b, left, and Supplementary Movie 2). Comparison of clusters 1 and 3 in Int1, along the first principal mode, showed a flattening of the angle between the headpiece and lower legs (Figure 5b, right, and Supplementary Movie 3). These motions were independent from one another. From the Int2 simulations, we identified two clusters (Figure 4c and Supplementary Movie 4), along the first principal mode. Analysis of residue positions showed that the region containing the ligand binding site twists, combined with further lengthening of the headpiece and changes in the orientation of the transmembrane β helix (Figure 5c). These emergent motions were coordinated (Figure 4c). For open $\alpha_{IIb}\beta_3$, we found three clusters (Figure 4d). The ectodomain was highly flexible, with pivoting of the headpiece relative to the lower legs for $\alpha_{IIb}$ and of the whole ectodomain relative to the

transmembrane helices for $\beta_3$ (Figure 5d and Supplementary Movie 5). Transmembrane helices also changed orientation in the direction to maintain their alignment relative to the main axis of the ectodomain (Figure 5d and Supplementary Movie 5).

In summary, analysis of $\alpha_{IIb}\beta_3$ integrin conformations along the plane identified by the first two principal modes showed that bent integrin tends to move the ectodomain (Figure 5a). In Int1, the headpiece separates from the lower legs and the angle between them flattens, following two independent modes of motion (Figure 5b). In Int2, the headpiece further extends, the ligand binding interface rotates, and the transmembrane β helix reorients, resulting in three correlated modes of motion (Figure 5c). In the open conformation, both the ectodomain and transmembrane helices move along the first principal mode, with the β chain presenting the highest flexibility (Figure 5d).

Notably, conformational changes from bent to extended conformations start from the headpiece and are then transmitted to the transmembrane helices. In the initial intermediate conformation, the flattening of the angle between headpiece and lower legs and its extension in the vertical direction are independent motions, whereas in the second intermediate, the twisting of the ligand binding site, the extension of the headpiece and leg separation are all correlated motions. These correlations, in which elongation of the ectodomain is combined with movement of its ligand binding site and reorientation of the transmembrane β helix, are likely to underlie the coordinated binding of an external ligand and accessory cytoplasmic proteins. Additionally, the motions of the transmembrane helices increase as integrin extends, propagating from the transmembrane β helix to the transmembrane α helix.

389

390 **Brownian dynamics simulations of integrin adhesion assembly**

391 We next assessed the effect of $\alpha_{IIb}\beta_3$ integrin conformation on the assembly of
392 nascent adhesions by incorporating different integrin conformations into a mesoscale
393 model (schematics in Figure S1a). Our results showed a monotonic increase of ligand-
394 bound integrins, from about 30% for the bent conformation to more than 90% for the fully
395 open conformation, as their $k_{on}$ and $\tau_{MAX}$ increased (Figure 6a). The enhanced ligand
396 binding of integrins was promoted by increases in ligand-bound lifetimes, which shifted
397 the transition from unstable to stable adhesions towards lower values of $k_{on}$ (Figure 6a
398 and Figure S7). A threshold $k_{on}$, indicating at which adhesion stability was achieved,
399 decreased with ligand density and ligand-bound lifetimes (Figure 6b and Figure S8).
400 Increases in ligand-binding affinity, which depends on the relation between $k_{on}$ and $k_{off}$ led
401 to adhesion stability (Figure 6c). At all values of $\tau$, an increase in free energy for ligand
402 binding from 1 to 2 $k_BT$ corresponded to a shift from unstable to stable adhesions (Figure
403 6c). Collectively, these data indicate that integrin conformation, corresponding to a
404 specific combination of $k_{on}$ and $\tau_{MAX}$, governs adhesion stability depending on ligand
405 density.

406 We then ran simulations incorporating $k_{on}$ and $\tau_{MAX}$ representing each $\alpha_{IIb}\beta_3$
407 integrin conformation. The distribution of average ligand-bound integrins shifted toward
408 higher values as conformation shifted from bent to extended (Figure 6d). Additionally,
409 using a constant density of 300 ligands/$\mu m^2$, the distribution of bound integrins narrowed
410 from bent to extended states (Figure 6d), with less variability in the amount of ligand

binding at high affinities (high $k_{on}$) and high ligand-bound lifetimes (low $k_{off}$, or high $\tau_{MAX}$). Consistent with more ligand-bound integrins, the average minimum distance between ligand-bound integrins was larger than 90 nm for bent integrin and less than 60 nm for intermediate and open $\alpha_{IIb}\beta_3$ conformations (Figure 6e), indicating that the probability of adhesion stabilization was high for intermediate and open integrins and low for bent integrins. This result is consistent with previous findings of weak adhesions from bent integrins and robust adhesions from intermediate and open conformations (54). Collectively, these results showed that closed/bent $\alpha_{IIb}\beta_3$ fails to stabilize nascent adhesions, whereas conversion to the intermediate states promotes adhesion stability nearly (Int1) or as well (Int2) as the open conformation. This finding implies that the force from binding ligands can convert integrin conformation from partially open to fully open conformations. Importantly, our model demonstrates that a small increases in integrin affinity of less than 1 $k_BT$ corresponds to a transition from unstable to stable adhesions. Ligand density influences where the transition from unstable to stable adhesion occurs, and thus at which integrin conformation stabilization can be achieved (Figure S8).

## Discussion

Integrins transition from bent, low affinity to extended, high affinity conformations through intermediate conformations, which influence cell adhesive function (8, 10, 13, 16, 54, 55). However, the properties of these conformations and their roles in adhesion assembly remain largely unexplored. In this study, we ran MD simulations on four $\alpha_{IIb}\beta_3$ conformations and extracted their essential dynamics through PCA. Our results indicated

that conformational fluctuations of $\alpha_{IIb}\beta_3$ integrin are enhanced in the intermediate and open conformations with respect to the bent conformation. Mesoscale modeling further allowed us to evaluate the role of different integrin conformations in cell adhesion assembly and identified a mechanism linking conformations of integrin to stabilization of nascent adhesions.

Analysis of the MD trajectories suggested that conformational activation of integrin progresses through stages of increasing domain fluctuations, except for the β-I and β-T domains, presenting enhanced fluctuations at the onset of headpiece extension (Figure 2c). These fluctuations may originate from the loss of molecular contacts and regulation of a “deadbolt” locking β-I in the inactive state of bent integrin (56).

PCA of $\alpha_{IIb}\beta_3$ integrins indicated that most molecular fluctuations are contained along a limited number of principal modes (Figure 3). These modes correspond to collective displacements in the directions of knee flattening, headpiece extension and leg separation (Figure 4-5). Interestingly, these modes varied significantly between the different $\alpha_{IIb}\beta_3$ integrin conformaitons, with independent uncoupled motions of the first intermediate and coupled deformations between headpiece and legs for the more extended intermediate and the open conformations. We have previously shown that force promotes integrin conformational activation, depending upon its molecular structure and activating mutant (15). It is plausible that the different modes of deformation that are associated with the different molecular structures underlie different structural responses to force. It would be interesting to evaluate, in the future, how the mutants perturb these modes of motion.

Identification of conformational clusters suggested that headpiece extension and leg separation occur sequentially, as previously proposed (11). Uncoupled motions of the headpiece are transmitted to the β helix first and then to the α helix. In the bent and first intermediate conformations, only motions of the ectodomain were observed. In the first intermediate, headpiece extension in the vertical direction proceeded independently from flattening of the angles between headpiece and lower legs. In the later phases of activation, corresponding to the second intermediate and open conformations, the rearrangements of the headpiece, including exposure of its ligand binding site, separation between the α and β chains, and legs opening were coupled.

The result that the essential dynamics of $\alpha_{IIb}\beta_3$ integrin occurs with motions of selected parts of the protein demonstrates that these motions are intrinsic properties of integrin and do not dependent on ligand binding, applied forces or interactions with plasma membrane lipids (Figure S3-5). This finding supports previous observations that conformational activation is an inherent property of the integrin itself and can proceed in the absence of signal transduction events (57). Our results also revealed that ligand or force on the bent conformation enhances residue motions (Figure S3-S4) by providing the energy to escape from the deep energy well; however, the most favored directions are still encoded within the conformartions and maintained in the absence of lipids (Figure S5). Interestingly, the fully open conformation is unstable; external stimuli may therefore have an opposite effect, stabilizing this state. This notion points towards a view of different integrin conformations as states with different physical properties, with each one possessing a distinct conformational signature.

Our equilibrium simulations, without a bound ligand and force, capture physiologically relevant conditions, as $\alpha_{IIb}\beta_3$ integrins in partially extended conformations have been experimentally observed without a bound ligand (58, 59). In platelets that are activated with agonists such as ADP, thrombin or arachidonic acid, integrin $\alpha_{IIb}\beta_3$ transitions from bent to extended states before ligand binding. The use of divalent cations (e.g. $Mg^{2+}$, $Mn^{2+}$), activation-associated mutations and activating antibodies (e.g. CBR LFA1/2), and intracellular activators such as overexpressed talin head domain also promote integrin conformational activation prior to ligand binding (24, 54, 57, 60–63).

Calculation of the extensional stiffness of the $\alpha_{IIb}\beta_3$ integrins showed that the bent conformation is the stiffest and the open conformation is the most flexible, with the intermediates in between (Figure 3c and Figure S7). This result is opposite to the trend captured using a ligand-coated biomembrane force probe where ligand binding was a prerequisite for the measurements (8, 14, 64). Additionally, our data are either one or two orders of magnitude higher than reported values (8, 14, 64). In our simulations, the bent conformation is the stiffest because it has a high energy barrier for transitioning into an extended state; the intermediate conformations are more flexible, presenting a lower energy barrier than the bent conformation. It follows that the open conformation is the most flexible. In fact, when force is applied to bent intergin, we observed higher flexibility and higher residue fluctuations relative to force-free conditions (Figure S3a-c). These results depend, in part, on the force- and ligand- free conditions used in our simulations versus experiments. Additionally, force probe experiments measured the net movement of the whole protein, whereas our simulations considered local residue movements (equations 1 and 2). Stiffness values from our simulations govern the energy well that

maintain integrin in a specific conformational state. Therefore, values from our simulations may not be relevant to the deformation of the whole integrin structure in experiments.

Mesoscale modeling further identifies a mechanism linking integrin conformation to the stabilization of adhesions. According to this model, bent integrins can bind ligands with low affinity, but short bond lifetimes prevent adhesion stabilization. As the integrin headpiece extends, the probability of ligand binding increases and once bound, the increase in bond lifetime confers stability. Therefore, increases in integrin affinity across intermediate conformations stabilize nascent adhesions via an increase in the duration of the integrin-ligand bond. These effects are also dependent on ligand density, with higher density/closer lateral proximity stabilizing adhesions at lower values of affinity (Figure S8), consistent with experimental studies (42–47). Our results additionally identify a minimum affinity threshold for conferring stability, such that below this threshold, achievable ligand densities are unable to confer stability (Figure S8). Live cell experiments in which integrin conformation, and thus ligand binding affinity, is fixed at different stages of activation are needed to evaluate the exact relationship between ligand density, affinity, on- and off-rates and adhesion stability.

Our BD simulations did not consider transitions across conformations over time. If a bent or intermediate integrin shift its conformation to a more extended state upon ligand binding, then adhesion stabilization would occur at lower values of initial affinity and ligand-bond lifetimes. While our analysis focused on $\alpha_{IIb}\beta_3$, these principles are likely applicable to other integrins.

This study leads to two main conclusions of high novelty. First, the combination of simulation approaches demonstrates that, in the absence of ligand binding, headpiece motions precede leg motions and fluctuations of the transmembrane β helix precede those of the transmembrane α helix. The initial headpiece motions can be related to early increases in ligand binding affinity upon destabilization of the bent conformation that are not reflected by significant headpiece extension (11). The motions that are transmitted from the headpiece to the β transmembrane helix are likely important for binding of accessory cytoplasmic proteins, connection with the cytoskeleton and intracellular signaling. Second, our results identify a new mechanism by which small changes in affinity are transduced into adhesion stabilization through control of the molecular integrin-ligand catch bond. The importance of the ligand-bond lifetime in adhesion stabilization has previously been reported from studies of cell spreading (31, 32), but has not been investigated in relation with integrin conformation.

These results raise a few questions that remain to be addressed in future work. How binding of intracellular adaptor proteins to cytoplasmic domains affect integrin conformational transitions is critical, as are the effects of the proteins on integrin clustering versus affinity (65–69). Additionally, since substrate rigidity plays an important role in integrin conformational activation and ligand-bound lifetime (31), it will be interesting to test the effect of substrate stiffness on adhesion assembly through conformational changes of integrin and affinity maturation.

## Acknowledgments

This work was supported by the Huntsman Cancer Institute and Scientific Computing and Imaging Institute CORI funding to T.C.B. Computer time was provided by the Scientific Computing and Imaging Institute and the Center for High Performance Computing at the University of Utah. MAS and TAB were supported by the National Science Foundation Grant NSF BMMB 2044394.

**Declaration of interests:** The authors declare no competing interests.

**Author contributions**: T.C.B designed the research; D.T., N.S. and R.K. performed the research; D.T., N.S. and R.K. analyzed the data. M.A.S. provided critical input concerning data interpretation. D.T., N.S., M.A.S. and T.C.B wrote the paper.

## Figure legends

**Figure 1. All atom representations of $\alpha_{IIb}\beta_3$ integrin conformations and insertion of the missing residues in bent integrin.** Ribbon representation of the atomistic structures of the four $\alpha_{IIb}\beta_3$ integrin conformations, with the α chain in green and the β chain in cyan: (a) bent; (b) int1; (c) int2; and (d) open conformations. (e) Schematic representation of open integrin with the domains of the α and β chains indicated. (f) Side view of bent integrin embedded in the lipid bilayer. (g) Ribbon representation of bent integrin with the α chain in green and the β chain in cyan. The three missing regions are shown in red loops. (h-l) Zoom-in view of the three reconstructed regions: (h) residue 840-873 in α chain; (i) residue 75-78 in β chain; (j) residue 764-774 in α chain.

**Figure 2. Analysis of atomistic MD simulation trajectories of four $\alpha_{IIb}\beta_3$ integrin conformations.** (a) The Cα RMSD of the four $\alpha_{IIb}\beta_3$ integrins relative to the corresponding input conformations over the course of 500 ns of atomistic MD simulations. (b) Radius of gyration of the four $\alpha_{IIb}\beta_3$ integrins over the course of 500 ns of atomistic MD simulations. (c) RMSF, computed for each integrin domain relative to its average position during the atomistic MD simulations. Errorbars indicate the standard deviations from the mean.

**Figure 3. PCA analysis and evaluation of atomistic MD fluctuations.** (a) Cumulative variance of Cα fluctuations for the four integrin conformations as a function of the principal components from 1 to 10. Data were extracted from the Cα trajectories during 500 ns of equilibrium MD simulations. (b) Fluctuations between the headpiece and lower legs of the four $\alpha_{IIb}\beta_3$ integrin conformations for the first 10 modes, calculated between 200 and 400 ns of equilibrium MD simulations. The values were obtained from evaluation of the fluctuations in distance between headpiece and lower legs from the principal modes. (c) Extensional stiffness of the four $\alpha_{IIb}\beta_3$ integrins from PCA of the equilibrium atomistic MD between 200 ns to 400 ns. The stiffness corresponding to the number of components having a cumulative variance of more than 95% was chosen for each integrin conformation. (d) Average distance of the headpiece from the legs, computed between the pulling group (residues: E220, S121, S123, D119, D251 in the MIDAS domain, D217, N215, D158, P219 in the LIMBS domain and D126, D127, M335 in the ADMIDAS domain) and the reference group (residues: W967-W988 in the α chain and V696-W715 in the β chain).

**Figure 4. Projection of MD simulation trajectories to the first two PCA modes**. The scatter plots of simulation frame projections are colored by their simulation times, and the clusters are indicated with green, red, and magenta for clusters 1, 2 and 3, respectively. (a) Bent integrin presented two clusters, centered at (0, 0) and (-4600, 2400), respectively. Structures representative of these two clusters were extracted at time step 456.9 ns and 353.1 ns. (b) Int1 presenetd four clusters, centered at (450, 450), (300, -2000), (-5200, 850) and (-5500, -1500). Representative structures of each cluster were

extracted at time step 359.1ns, 471.7ns, 134.4ns and 485.9ns. (c) Int2 presented two clusters, centered at (3000, 0) and (-4000, 0). Representative structures were extracted at 295.1ns and 101.1ns. (d) Open $\alpha_{IIb}\beta_3$ presented three clusters, centered at (6500, 400), (-1000, 200) and (400, -2500), respectively. Representative structures were extracted at 28.2ns, 445.9ns and 45.8ns.

**Figure 5. Representative structures from clusters identified on the plane of the first two principal modes.** (a) Superposition of the representative atomistic structures from clusters 1 and 2 in the bent states. (b) Superposition of the representative structures from clusters 1, 2 and 3 in int1. (c) Superposition of the representative structures from clusters 1 and 2 in int2. (d) Superposition of the representative structures from clusters 1 and 2. The atomistic structures are colored in green, red and magenta for cluster 1, 2 and 3, respectively.

**Figure 6. Integrin conformation determines the density of ligand-bound integrins in nascent adhesions.** (a) Average percentage of ligand-bound integrins increasing ligand binding affinity and, simultaneously, maximum lifetime of the ligand-bound state, $\tau_{MAX}$, as well as the force corresponding to $\tau_{MAX}$. Data were extracted between 200 s and 300 s of simulations, using 300 ligands/μm$^2$ and $Y$=12.6 kPa. (b) Threshold in $k_{on}$ for the transition between unstable and stable adhesion as a function of $\tau_{MAX}$ and ligand density. Data were extracted between 200 s and 300 s of simulations, using 100, 200 and 500 ligands/μm$^2$ and $Y$=12.6 kPa. (c) Average smallest distance between ligand-bound integrins as a function of ligand binding affinity, $E$. Ligand binding affinity was calculated

620 from $\frac{k_{off}}{k_{on}} = e^{-E}$, in units of $k_BT$, where $k_B$ is Boltzmann's constant, and $T$ is the
621 temperature. Data were extracted between 100 s and 300 s of simulations, using 300
622 ligands/μm$^2$ and $Y$=12.6 kPa. (d) Boxplots of ligand-bound integrins for the different
623 integrin conformations: bent was represented by $k_{on}$ = 0.05s$^{-1}$, $\tau_{MAX}$= 6 s, and force
624 corresponding to $\tau_{MAX}$ around 18 pN; int1 was modeled using $k_{on}$ = 0.7 s$^{-1}$, $\tau_{MAX}$= 11 s
625 and $\tau_{MAX}$ force of 30 pN; open and int2 were modeled using $k_{on}$ = 1 s$^{-1}$ and $\tau_{MAX}$= 22 s,
626 with force corresponding to $\tau_{MAX}$ around 40 pN. Data were extracted between 200 s and
627 300 s of simulations, using 300 ligands/$\mu m^2$ and $Y$=12.6 kPa. (e) Average smallest
628 distance between ligand-bound integrins. Errorbars represent standard deviation from the
629 mean. Data were extracted between 260 s and 300 s of simulations, using 300
630 ligands/$\mu m^2$ and $Y$ = 12.6 kPa.

631

632 **References**


633 1. Ma, Y.-Q., J. Qin, and E.F. Plow. 2007. Platelet integrin alpha(IIb)beta(3): activation
634 mechanisms. *J Thromb Haemost*. 5:1345–52.
635 2. Botero, J.P., K. Lee, B.R. Branchford, P.F. Bray, K. Freson, M.P. Lambert, M. Luo, S.
636 Mohan, J.E. Ross, W. Bergmeier, J. di Paola, and ClinGen Platelet Disorder Variant
637 Curation Expert Panel. 2020. Glanzmann thrombasthenia: genetic basis and clinical
638 correlates. *Haematologica*. 105:888–894.
639 3. Tello-Montoliu, A., E. Jover, J. Rivera, M. Valdés, D.J. Angiolillo, and F. Marín. 2012.
640 New perspectives in antiplatelet therapy. *Curr Med Chem*. 19:406–27.
641 4. Xiong, J.P., T. Stehle, B. Diefenbach, R. Zhang, R. Dunker, D.L. Scott, A. Joachimiak,
642 S.L. Goodman, and M.A. Arnaout. 2001. Crystal structure of the extracellular segment of
643 integrin alpha Vbeta3. *Science*. 294:339–45.
644 5. Xiong, J.-P., T. Stehle, R. Zhang, A. Joachimiak, M. Frech, S.L. Goodman, and M.A.
645 Arnaout. 2002. Crystal structure of the extracellular segment of integrin alpha Vbeta3 in
646 complex with an Arg-Gly-Asp ligand. *Science*. 296:151–5.
647 6. Zhu, J., J. Zhu, and T.A. Springer. 2013. Complete integrin headpiece opening in eight
648 steps. *J Cell Biol*. 201:1053–68.
649 7. Zhou, D., A.M.M. Thinn, Y. Zhao, Z. Wang, and J. Zhu. 2018. Structure of an extended
650 β3 integrin. *Blood*. 132:962–972.
651 8. Chen, Y., L.A. Ju, F. Zhou, J. Liao, L. Xue, Q.P. Su, D. Jin, Y. Yuan, H. Lu, S.P. Jackson,
652 and C. Zhu. 2019. An integrin α(IIb)β(3) intermediate affinity state mediates
653 biomechanical platelet aggregation. *Nat Mater*. 18:760–769.
654 9. Kamata, T., M. Handa, Y. Sato, Y. Ikeda, and S. Aiso. 2005. Membrane-proximal
655 {alpha}/{beta} stalk interactions differentially regulate integrin activation. *J Biol Chem*.
656 280:24775–24783.
657 10. Chen, X., C. Xie, N. Nishida, Z. Li, T. Walz, and T.A. Springer. 2010. Requirement of
658 open headpiece conformation for activation of leukocyte integrin alphaXbeta2. *Proc Natl*
659 *Acad Sci U S A*. 107:14727–14732.
660 11. Coutinho, A., C. García, J. González-Rodríguez, and M.P. Lillo. 2007. Conformational
661 changes in human integrin alphaIIbbeta3 after platelet activation, monitored by FRET.
662 *Biophys Chem*. 130:76–87.
663 12. Xiao, T., J. Takagi, B.S. Coller, J.-H. Wang, and T.A. Springer. 2004. Structural basis for
664 allostery in integrins and binding to fibrinogen-mimetic therapeutics. *Nature*. 432:59–67.
665 13. Luo, B.-H., C. v Carman, and T.A. Springer. 2007. Structural basis of integrin regulation
666 and signaling. *Annu Rev Immunol*. 25:619–47.
667 14. Chen, W., J. Lou, E.A. Evans, and C. Zhu. 2012. Observing force-regulated
668 conformational changes and ligand dissociation from a single integrin on cells. *J Cell Biol*.
669 199:497–512.
670 15. Driscoll, T.P., T.C. Bidone, S.J. Ahn, A. Yu, A. Groisman, G.A. Voth, and M.A.
671 Schwartz. 2021. Integrin-based mechanosensing through conformational deformation.
672 *Biophys J*. 120:4349–4359.

16. Cormier, A., M.G. Campbell, S. Ito, S. Wu, J. Lou, J. Marks, J.L. Baron, S.L. Nishimura, and Y. Cheng. 2018. Cryo-EM structure of the αvβ8 integrin reveals a mechanism for stabilizing integrin extension. *Nat Struct Mol Biol*. 25:698–704.
17. Takagi, J., B.M. Petre, T. Walz, and T.A. Springer. 2002. Global conformational rearrangements in integrin extracellular domains in outside-in and inside-out signaling. *Cell*. 110:599–11.
18. Xu, X.-P., E. Kim, M. Swift, J.W. Smith, N. Volkmann, and D. Hanein. 2016. Three-Dimensional Structures of Full-Length, Membrane-Embedded Human α(IIb)β(3) Integrin Complexes. *Biophys J*. 110:798–809.
19. Fiser, A., R.K. Do, and A. Sali. 2000. Modeling of loops in protein structures. *Protein Sci*. 9:1753–1773.
20. Abraham, M.J., T. Murtola, R. Schulz, S. Páll, J.C. Smith, B. Hess, and E. Lindah. 2015. Gromacs: High performance molecular simulations through multi-level parallelism from laptops to supercomputers. *SoftwareX*. 1–2:19–25.
21. Jo, S., J.B. Lim, J.B. Klauda, and W. Im. 2009. CHARMM-GUI Membrane Builder for Mixed Bilayers and Its Application to Yeast Membranes. *Biophys J*. 97:50–58.
22. Lau, T.-L., C. Kim, M.H. Ginsberg, and T.S. Ulmer. 2009. The structure of the integrin alphaIIbbeta3 transmembrane complex explains integrin transmembrane signalling. *EMBO J*. 28:1351–61.
23. Lau, T.-L., V. Dua, and T.S. Ulmer. 2008. Structure of the integrin alphaIIb transmembrane segment. *J Biol Chem*. 283:16162–8.
24. Shattil, S.J., C. Kim, and M.H. Ginsberg. 2010. The final steps of integrin activation: the end game. *Nat Rev Mol Cell Biol*. 11:288–300.
25. Jorgensen, W.L., J. Chandrasekhar, J.D. Madura, R.W. Impey, and M.L. Klein. 1983. Comparison of simple potential functions for simulating liquid water. *J Chem Phys*.
26. Parrinello, M., and A. Rahman. 1981. Polymorphic transitions in single crystals: A new molecular dynamics method. *J Appl Phys*.
27. Hess, B., H. Bekker, H.J.C. Berendsen, and J.G.E.M. Fraaije. 1997. LINCS: A linear constraint solver for molecular simulations. *J Comput Chem*. 18:1463–1472.
28. Darden, T., D. York, and L. Pedersen. 1993. Particle mesh Ewald: An N·log(N) method for Ewald sums in large systems. *J Chem Phys*.
29. Humphrey, W., A. Dalke, and K. Schulten. 1996. VMD: Visual molecular dynamics. *J Mol Graph*. 14:33–38.
30. Delano, W.L. 2002. The PyMOL Molecular Graphics System. .
31. Oakes, P.W., T.C. Bidone, Y. Beckham, A.V. Skeeters, G.R. Ramirez-San Juan, S.P. Winter, G.A. Voth, and M.L. Gardel. 2018. Lamellipodium is a myosin-independent mechanosensor. *Proc Natl Acad Sci U S A*. 115.
32. Bidone, T.C., A. v. Skeeters, P.W. Oakes, and G.A. Voth. 2019. Multiscale model of integrin adhesion assembly. *PLoS Comput Biol*.
33. Rossier, O., V. Octeau, J.-B. Sibarita, C. Leduc, B. Tessier, D. Nair, V. Gatterdam, O. Destaing, C. Albigès-Rizo, R. Tampé, L. Cognet, D. Choquet, B. Lounis, and G. Giannone. 2012. Integrins β1 and β3 exhibit distinct dynamic nanoscale organizations inside focal adhesions. *Nat Cell Biol*. 14:1057–1067.
34. Califano, J.P., and C.A. Reinhart-King. 2010. Substrate Stiffness and Cell Area Predict Cellular Traction Stresses in Single Cells and Cells in Contact. *Cell Mol Bioeng*. 3:68–75.

35. Han, S.J., K.S. Bielawski, L.H. Ting, M.L. Rodriguez, and N.J. Sniadecki. 2012. Decoupling substrate stiffness, spread area, and micropost density: a close spatial relationship between traction forces and focal adhesions. *Biophys J*. 103:640–648.
36. Tee, S.-Y., J. Fu, C.S. Chen, and P.A. Janmey. 2011. Cell shape and substrate rigidity both regulate cell stiffness. *Biophys J*. 100:L25-7.
37. Engler, A., L. Bacakova, C. Newman, A. Hategan, M. Griffin, and D. Discher. 2004. Substrate Compliance versus Ligand Density in Cell on Gel Responses. *Biophys J*.
38. Kubo, R. 1966. The fluctuation-dissipation theorem. *Reports on Progress in Physics*. 29:255–284.
39. Bell, G.I. 1978. Models for the specific adhesion of cells to cells. *Science (1979)*.
40. Chakraborty, S., D. Chaudhuri, D. Chaudhuri, V. Singh, S. Banerjee, D. Chowdhury, and S. Haldar. 2022. Connecting conformational stiffness of the protein with energy landscape by a single experiment. *Nanoscale*. 14:7659–7673.
41. 2016. Differential and Difference Equations. *Numerical Methods for Ordinary Differential Equations*. 1–53.
42. Deeg, J.A., I. Louban, D. Aydin, C. Selhuber-Unkel, H. Kessler, and J.P. Spatz. 2011. Impact of local versus global ligand density on cellular adhesion. *Nano Lett*. 11:1469–76.
43. Cavalcanti-Adam, E.A., T. Volberg, A. Micoulet, H. Kessler, B. Geiger, and J.P. Spatz. 2007. Cell Spreading and Focal Adhesion Dynamics Are Regulated by Spacing of Integrin Ligands. *Biophys J*. 92:2964–2974.
44. Moore, S.W., P. Roca-Cusachs, and M.P. Sheetz. 2010. Stretchy proteins on stretchy substrates: the important elements of integrin-mediated rigidity sensing. *Dev Cell*. 19:194–206.
45. Arnold, M., E.A. Cavalcanti-Adam, R. Glass, J. Blümmel, W. Eck, M. Kantlehner, H. Kessler, and J.P. Spatz. 2004. Activation of integrin function by nanopatterned adhesive interfaces. *Chemphyschem*. 5:383–8.
46. Koo, L.Y., D.J. Irvine, A.M. Mayes, D.A. Lauffenburger, and L.G. Griffith. 2002. Co-regulation of cell adhesion by nanoscale RGD organization and mechanical stimulus. *J Cell Sci*. 115:1423–33.
47. Schvartzman, M., M. Palma, J. Sable, J. Abramson, X. Hu, M.P. Sheetz, and S.J. Wind. 2011. Nanolithographic control of the spatial organization of cellular adhesion receptors at the single-molecule level. *Nano Lett*. 11:1306–12.
48. David, C.C., and D.J. Jacobs. 2014. Principal component analysis: a method for determining the essential dynamics of proteins. *Methods Mol Biol*. 1084:193–226.
49. Amadei, A., A.B. Linssen, and H.J. Berendsen. 1993. Essential dynamics of proteins. *Proteins*. 17:412–25.
50. Michaud-Agrawal, N., E.J. Denning, T.B. Woolf, and O. Beckstein. 2011. MDAnalysis: a toolkit for the analysis of molecular dynamics simulations. *J Comput Chem*. 32:2319–27.
51. Gowers, R., M. Linke, J. Barnoud, T. Reddy, M. Melo, S. Seyler, J. Domański, D. Dotson, S. Buchoux, I. Kenney, and O. Beckstein. 2016. MDAnalysis: A Python Package for the Rapid Analysis of Molecular Dynamics Simulations. . pp. 98–105.
52. Shimaoka, M., J. Takagi, and T.A. Springer. 2002. Conformational regulation of integrin structure and function. *Annu Rev Biophys Biomol Struct*. 31:485–516.
53. Selhuber-Unkel, C., M. López-García, H. Kessler, and J.P. Spatz. 2008. Cooperativity in adhesion cluster formation during initial cell adhesion. *Biophys J*. 95:5424–5431.

54. Salas, A., M. Shimaoka, U. Phan, M. Kim, and T.A. Springer. 2006. Transition from rolling to firm adhesion can be mimicked by extension of integrin αLβ2 in an intermediate affinity state. *Journal of Biological Chemistry*. 281:10876–10882.
55. Springer, T.A., and M.L. Dustin. 2012. Integrin inside-out signaling and the immunological synapse. *Curr Opin Cell Biol*. 24:107–115.
56. Xiong, J.-P., T. Stehle, S.L. Goodman, and M.A. Arnaout. 2003. New insights into the structural basis of integrin activation. *Blood*. 102:1155–9.
57. O'Toole, T.E., J.C. Loftus, X.P. Du, A.A. Glass, Z.M. Ruggeri, S.J. Shattil, E.F. Plow, and M.H. Ginsberg. 1990. Affinity modulation of the alpha IIb beta 3 integrin (platelet GPIIb-IIIa) is an intrinsic property of the receptor. *Cell Regul*. 1:883–93.
58. Humphries, M.J. 2004. Monoclonal antibodies as probes of integrin priming and activation. *Biochem Soc Trans*. 32:407–411.
59. Humphries, M.J., P.A. McEwan, S.J. Barton, P.A. Buckley, J. Bella, and A.P. Mould. 2003. Integrin structure: heady advances in ligand binding, but activation still makes the knees wobble. *Trends Biochem Sci*. 28:313–20.
60. Kim, C., F. Ye, and M.H. Ginsberg. 2011. Regulation of Integrin Activation. *Annu Rev Cell Dev Biol*.
61. Shimaoka, M., and T.A. Springer. 2003. Therapeutic antagonists and conformational regulation of integrin function. *Nat Rev Drug Discov*. 2:703–16.
62. Huang, J., X. Li, X. Shi, M. Zhu, J. Wang, S. Huang, X. Huang, H. Wang, L. Li, H. Deng, Y. Zhou, J. Mao, Z. Long, Z. Ma, W. Ye, J. Pan, X. Xi, and J. Jin. 2019. Platelet integrin αIIbβ3: signal transduction, regulation, and its therapeutic targeting. *J Hematol Oncol*. 12:26.
63. Nishida, N., C. Xie, M. Shimaoka, Y. Cheng, T. Walz, and T.A. Springer. 2006. Activation of leukocyte beta2 integrins by conversion from bent to extended conformations. *Immunity*. 25:583–94.
64. Chen, Y., H. Lee, H. Tong, M. Schwartz, and C. Zhu. 2017. Force regulated conformational change of integrin αVβ3. *Matrix Biology*.
65. Bunch, T.A. 2010. Integrin alphaIIbbeta3 activation in Chinese hamster ovary cells and platelets increases clustering rather than affinity. *J Biol Chem*. 285:1841–9.
66. Helsten, T.L., T.A. Bunch, H. Kato, J. Yamanouchi, S.H. Choi, A.L. Jannuzi, C.C. Féral, M.H. Ginsberg, D.L. Brower, and S.J. Shattil. 2008. Differences in regulation of Drosophila and vertebrate integrin affinity by talin. *Mol Biol Cell*. 19:3589–98.
67. Abrams, C., Y.J. Deng, B. Steiner, T. O'Toole, and S.J. Shattil. 1994. Determinants of specificity of a baculovirus-expressed antibody Fab fragment that binds selectively to the activated form of integrin alpha IIb beta 3. *J Biol Chem*. 269:18781–8.
68. Buensuceso, C., M. de Virgilio, and S.J. Shattil. 2003. Detection of integrin alpha IIbbeta 3 clustering in living cells. *J Biol Chem*. 278:15217–24.
69. Han, J., C.J. Lim, N. Watanabe, A. Soriani, B. Ratnikov, D.A. Calderwood, W. Puzon-McLaughlin, E.M. Lafuente, V.A. Boussiotis, S.J. Shattil, and M.H. Ginsberg. 2006. Reconstructing and Deconstructing Agonist-Induced Activation of Integrin αIIbβ3. *Current Biology*. 16:1796–1806.